**David Adaway** is a Computer Engineering major at the University of Memphis expecting to graduate in spring 2026. He is a member of the Helen Hardin Honors College, and he plans to pursue a master's degree after earning his bachelor's degree. He has been involved in research under the supervision of Dr. Chrysanthe Preza, Professor and Chair of the Electrical and Computer Engineering Department, since he joined her Vertically Integrated Projects team in fall 2022. He began using the Axio Imager.Z1 microscope in her lab since summer 2024.

**Chrysanthe Preza** is the Kanuri Professor and Chair of the Department of Electrical and Computer Engineering at the University of Memphis, where she joined in 2006. She received her D.Sc. degree in Electrical Engineering from Washington University in St. Louis in 1998. She leads the research in the Computational Imaging Research Laboratory. Since 2022, she is the founder and Director of the Vertically Integrated Projects (VIP) Program at the University of Memphis. Her research interests are imaging science, estimation theory, computational optical sensing and imaging applied to multidimensional multimodal light microscopy and hyperspectral imaging, and computational imaging enabled by deep learning. She received a CAREER award by the National Science Foundation in 2009, the Herff Outstanding Faculty Research Award in 2010 and 2015, and she was the recipient of the Ralph Faudree Professorship at the University of Memphis 2015-2018. Since 2018, she has been the recipient of the Ravi and Eleanor Kanuri Professorship. She was named Fellow of the SPIE in 2019 and Fellow of the Optica (OSA) in 2020. She served as Associate Editor for *IEEE Transactions on Computational Imaging*, as Topical Editor for Optica's *Applied Optics*, and as an Executive Editor for *Biological Imaging, Cambridge University Press.* She currently serves as an Editorial Board Member for *Journal of Imaging, Computational Imaging and Computational Photography section.*

Adaway and Preza's paper received a *QuaesitUM* outstanding paper award.

**David Adaway & Chrysanthe Preza**

Comparison of Two Three-Dimensional Imaging Approaches Used in Fluorescence Microscopy

**Faculty Sponsor**

Dr. Chrysanthe Preza

## Abstract

This study introduces readers to fluorescence microscopy, the study of imaging biological samples that emit light when excited by light at specific wavelengths. A ZEISS Axio Imager.Z1 microscope was used to image an eosin-stained brine shrimp sample by *optical sectioning*, capturing the sample's full 3D depth in a widefield image stack. However, due to blurring caused by the microscope's point spread function (PSF), more complex imaging approaches must be used to obtain accurate images. This study focuses on two such approaches: deconvolution, applying a post-processing algorithm to remove the PSF from the widefield image; and structured illumination microscopy, during which a structured illumination pattern (provided by the ApoTome.2 add-on hardware) is projected on the sample during acquisition so more information is captured through light modulation, leading to fast and accurate image reconstruction. Readers who are unfamiliar with these microscopy modes can learn and apply them in their own research.

## Introduction

Fluorescence microscopy is a subfield of microscopy often used when imaging biological samples [1]. These samples contain fluorophores: molecules that, when excited by certain wavelengths of light, will emit light at a different wavelength in return. A microscope can filter out the excitation wavelength so the resulting image only includes the emission wavelength; only materials that fluoresce will be visible, providing the greatest contrast between the labeled specimen and the background. Some samples (those that are autofluorescent) have natural light-emitting properties; other samples can be stained with fluorescent dyes for imaging purposes.

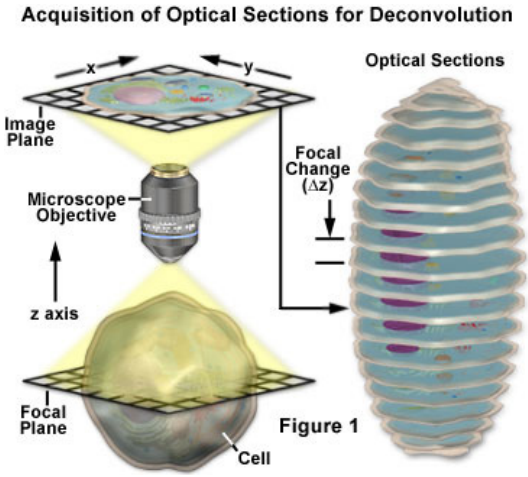


**Figure 1**.
3D image acquisition with uniform widefield microscopy [2].
One image of the subject is captured as a different part of the object is placed in the microscope's focal plane; the optical sections are stacked to form a 3D volume.

In a conventional light microscope, the sample is placed on a stage and illuminated by a lamp. For fluorescent samples, a filter is used to shift the light to the excitation wavelength. A two-dimensional (2D) image is then taken using a digital (CCD) camera integrated to the microscope, while the imaging lens is focused on the sample. This poses an issue for biological samples, many of which are three-dimensional (3D): in addition to the two lateral axes (X and Y), there is a third axis (Z) corresponding to the depth of the specimen, or the position within the specimen's thickness. One approach for imaging these samples is optical sectioning microscopy (OSM), where a 2D image is taken at each axial depth [3]. The depth is

changed by translating the stage vertically, which changes the part of the sample that is in focus by the microscope's objective, or imaging lens. The volume of the sample is represented by the "stack" of 2D images, or "slices" (Figure 1). For this method, the sample does not need to be specially prepared (besides the fluorescence staining, if necessary), and there is no risk of damage by physically sectioning it, unlike in electron microscopy for instance.

The drawback of optical sectioning microscopy is that each slice, also known as a widefield raw image, will contain both in-focus and out-of-focus light [3]. Emitted light from the entire volume is always visible to the objective, so regions of the sample that appear clear are mixed with regions that appear blurry; the position of the stage only changes which regions are in-focus. To obtain a clear depiction of a sample volume, the out-of-focus light must be removed from each slice.

The blurring from out-of-focus light can be modelled by a mathematical process called convolution, the integration of the product of the sample's emitted light and a shifted version of the microscope's point spread function (PSF), the microscope's response to a single point of light [4]. Each point of captured light is transformed according to the PSF (Figure 2); to remove out-of-focus light, the inverse process known as deconvolution must be performed. Widefield deconvolution microscopy uses the PSF to make educated guesses on the true appearance of the emitted light and solve the inverse imaging problem. There are different deconvolution algorithms of varying processing time and accuracy [5].

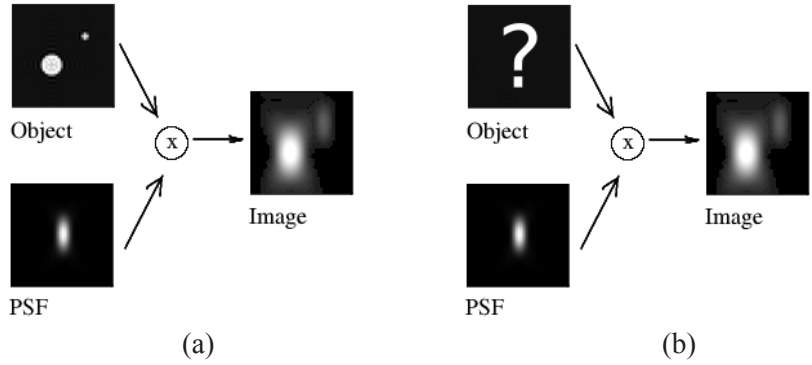


**Figure 2**.

(a) The output image is the convolution of the sampled object and the microscope's point spread function [6]. The PSF causes the light of the object to be redistributed accordingly. (b) In deconvolution, the image and the PSF are used to reconstruct the unknown object. The light transformation is reversed.

Alternatively, the optical sectioning process can be enhanced by structured illumination microscopy (SIM), removing the need for deconvolution. In SIM, a set of grid lines, or a structured illumination (SI) pattern, is applied on top of a 2D image (Figure 3). The SI pattern modulates the emitted light to different frequencies so that information that normally would not transfer through the widefield microscope can now be captured through this process. Each phase of the SI pattern (position of the grid lines) changes the modulation of light; thus, while summing the SIM images from different phases of the pattern results in a widefield image, image processing programs can extract information from each phase image and output a final result with improved optical sectioning [7]. The SIM process can be accomplished by taking multiple (usually, three to five) images at each axial depth of interest (the whole volume does not need to be processed) and using specialized microscope hardware to project a different SI pattern phase on each image. A computer program can then process the raw SIM data and output a new image at each chosen depth, improving the visual clarity of the image and the volume when a 3D image is desirable.

This study was performed by the primary author, an undergraduate student researcher, in order to learn about 3D fluorescence microscopy, image acquisition, computational image processing techniques, and data analysis. These are important preliminary skills necessary for future research inquiries. In addition, the work in this study was done in part to verify the correct operation of the equipment with a newer version of the commercial software, which was installed and tested for the experiments described below. As a demonstration of this work, this article will compare the processes and results obtained using conventional widefield deconvolution microscopy and optical sectioning structured illumination microscopy (OS-SIM, or simply "SIM" hereafter). First, the equipment used in this study and the actions taken to acquire the images are described. Then, various results from different processes are presented alongside technical explanations and visual observations. Finally, the images are directly compared (qualitatively and quantitatively) to determine the usefulness and application of each image restoration method.

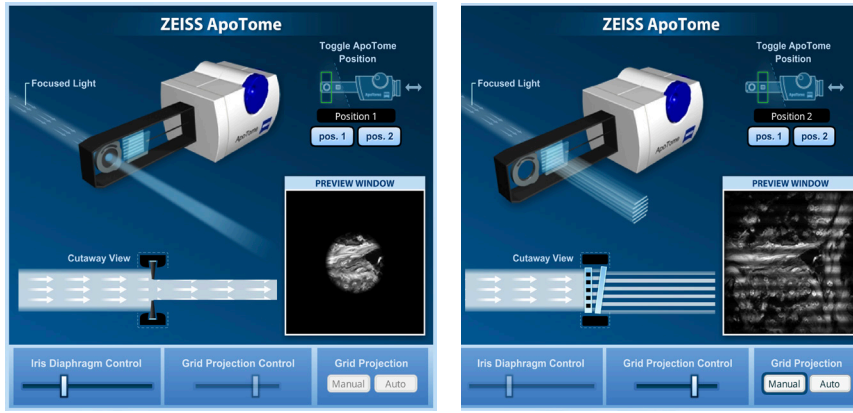


(a) (b)

**Figure 3**.

The ZEISS ApoTome add-on device creates a structured illumination pattern that can be integrated in widefield microscopy [8]. (a) In position 1, the ApoTome is not engaged; the illumination is uniform resulting in conventional widefield microscopy. (b) In position 2, focused light is split into sections, which are projected onto the sample object. Different phases of the illumination pattern are created by adjusting the angle of the reflective glass inside the ApoTome, causing the lines superimposed on the image (here displayed in the "Preview Window") to shift up and down.

## Methodology

This research study was performed in Dr. Chrysanthe Preza's Computational Imaging Research Laboratory (CIRL) in the Electrical and Computer Engineering Department at the University of Memphis. This is a computer-controlled microscopy experiment: specialized software is used to control the actions of the microscope. As part of this study, the undergraduate student contacted the microscope's manufacturer to obtain an updated version of the software; this required meetings with technical support to configure it correctly. Thanks to these preliminary steps, the microscope could be used for projects conducted in the CIRL. In this section, we will detail the actions taken to acquire, process, and prepare images using the tools available in our lab.

### *Tools and Parameters*

All data acquisition and processing was done on a fixed sample of a brine shrimp stained with the fluorescent dye eosin. Image acquisition was performed using a motorized Axio Imager.Z1 microscope (Figure 4a), manufactured by ZEISS Microscopy. The images were captured using an Ax-

ioCam MRm camera, the one shown above the eyepieces in Figure 4a; captured images have a resolution of 1388 x 1040 pixels. The ApoTome.2 add-on device (or simply "ApoTome" hereafter, Figure 4b) projects the SI patterns used by OS-SIM [7]. Computer control of the microscope was enabled by the ZEN 3.8 software for Windows, which was also produced by ZEISS Microscopy. ZEN was used to control the acquisition and restoration parameters (Figure 5). The computer that ran ZEN had an Intel Xeon X5650 CPU (clock speed of 2.66 GHz) with integrated graphics; the lack of a dedicated GPU had a significant effect on computational time.


(a) (b)

**Figure 4**.
(a) The Axio Imager.Z1 microscope (modified with a side imaging path for another research project in the CIRL) used for this study. (b) The ApoTome.2 add-on hardware.

All image restoration methods were performed on a single Z-Stack acquisition of the specimen, done with the ApoTome in position 2 (Figure 3b). Three excitation filters were used: Rhodamine, EGFP, and DAPI. The images were captured using the Plan-APOCHROMAT 20x/0.8 objective dry lens: the magnification is 20 and the numerical aperture is 0.8. With this objective, each pixel is a square of side length 0.3225 µm, so the axial step size was set to 0.32 µm (ZEN does not allow more precise settings) so the stack would contain cubic voxels. 184 slices were captured, and each slice contains five phase images due to the ApoTome's SI pattern. The axial range was chosen such that the middle slice (#92) would contain the most in-focus data while the first and last slices would be the most out-of-focus. The entire depth of the specimen was traversed by remotely translating the microscope stage (where the brine shrimp sample was set) using the ZEN software.

In the Z-Stack acquisition, the axial movement of the stage, the changing of the excitation filters, and the adjustment of the SI pattern are performed automatically. The output of the acquisition is a "Raw data" image stack containing the phase images for each slice and excitation filter (2,760 total images). Afterwards, we used ZEN's "Conventional Fluorescence" option to obtain the widefield stack and the "Optical sectioning" option to obtain the SIM-reconstructed stack; ZEN performs the respective computations on the raw data stack. The widefield images were digitally processed by applying three of the built-in deconvolution algorithms: Nearest Neighbor [9], Regularized Inverse Filter (RIF), and Conjugate Gradient Maximum Likelihood (CGML, or "Constrained Iterative") [10].

For the RIF and CGML deconvolution methods, the microscope's 3D point spread function (PSF) is required; the algorithms use the PSF to determine how the light was transformed during the convolution process (Figure 2). ZEN can generate the PSF automatically using acquisition metadata contained in the widefield data file. Alternatively, an external PSF can be provided; this would be done to input PSFs obtained by empirical measurements. In this study, an auto-generated PSF was used for RIF, and a PSF provided by an experienced research scientist (who developed CGML [10]) was used for CGML. We note that Nearest Neighbor uses a 2D PSF generated by ZEN, and OS-SIM does not require any PSF.

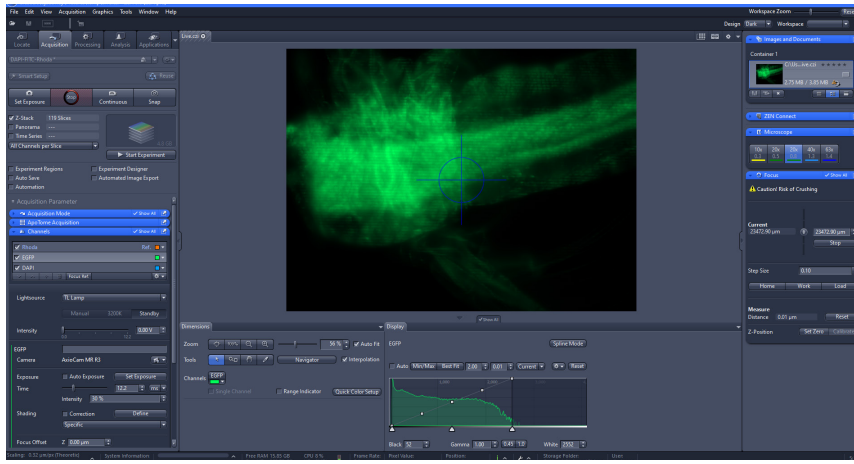

**Figure 5**.
The user interface of ZEN 3.8, the software used to control the acquisition. A live view of the microscope's camera is displayed. Illumination grid lines superimposed on the sample are evident in the image.

*Point Spread Function Generation*

For deconvolution, using an accurate point spread function (PSF) is important because the PSF acts as map for light between the sampled object and the image (Figure 2), much like a mathematical function $f$ with input $x$ and output $y$. In the same way it is impossible to solve the equation $y = f(x)$ for $x$ without knowledge of $f$, the sampled object cannot be accurately reconstructed without knowledge of PSF. Acquiring the PSF is the most important step of a deconvolution!

After performing an acquisition, metadata such as the numerical aperture, the wavelength of light, and the lateral and axial dimensions of the images are stored in the CZI (Carl Zeiss Image) format alongside the images themselves, so ZEN is able to automatically generate a corresponding PSF [11]. ZEN provides two algorithms for calculating a PSF based on a scalar model and a vectorial model. In general, the vectorial model is more accurate [12], but more difficult to compute via numerical methods, which sometimes can lead to artifacts, as demonstrated in Figure 6.

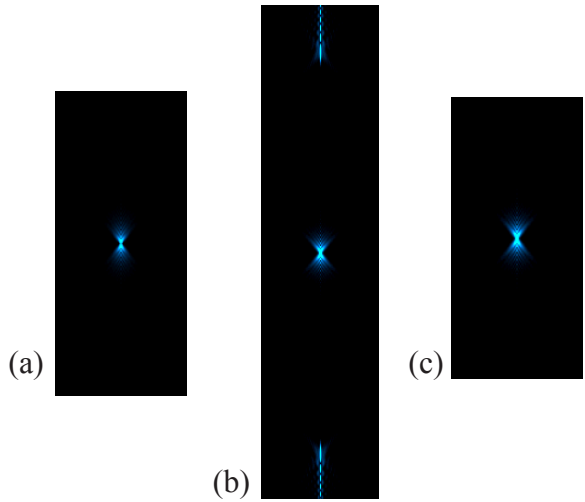


**Figure 6**.
Axial views of 3D PSFs (DAPI filter). (a) Scalar PSF for the widefield acquisition (Figure 7), generated by ZEN. (b) Vectorial PSF generated by ZEN. (c) Vectorial PSF supplied externally. Resolutions: (a) 109x240 pixels, (b) 109x454 pixels, (c) 109x218 pixels.

While the scalar PSF (Figure 6a) turned out aberration-free, the vectorial PSF (Figure 6b) has visible "tail-artifacts" at the top and bottom of the images. To obtain the highest-quality deconvolution, an expert re-

search scientist (co-developer of the CGML method [10]) was consulted; he provided a new vectorial PSF (Figure 6c), which was used to perform the CGML method. For the Regularized Inverse Filter deconvolution, we used the generated scalar PSF, while for the Nearest Neighbor a 2D PSF was used as noted above.

*Figure Preparation*

All results from ZEN were exported in the CZI format and imported into Fiji [13] (a distribution of the open-source imaging software ImageJ [14]) using its Bio-Formats Importer plugin [15]. Fiji was used for preparation of the figures presented here for image comparison and analysis. Each dataset (widefield, deconvolution results, and OS-SIM restoration) is an image stack containing 184 slices (traversing 58.56 microns of the sample's depth). Each slice has a resolution of 1388x1040 pixels (or 447.63x335.40 microns). Figures of the XY view in this paper depict slice #92, the middle slice. The XZ orthogonal views allow the sample's depth to be visualized: the x-axis increases rightward, and the z-axis increases downward. The XZ views are focused on Y = 520, the horizontal center of the XY view.

This study includes a qualitative and quantitative analysis and comparison of results from different image restoration methods. By examining intensity profiles and orthogonal views, each method's improvement over widefield microscopy is demonstrated.

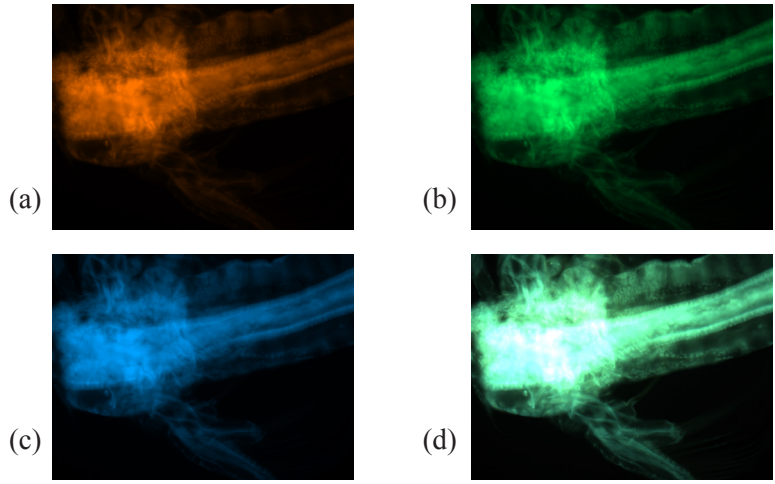


**Figure 7**.
XY views of acquired widefield image stacks, using the (a) Rhodamine, (b) EGFP, and (c) DAPI excitation filters. (d) Shows the composite image created from (a)-(c).

## Results

In this section, we explain the computational methodologies involved in the creation of each image. The results are compared by examining the images visually (qualitatively) and by examining their pixel intensities (quantitatively).

*Conventional Fluorescence*

The conventional fluorescence, or widefield, dataset studied here was obtained by summing the phase images from the ApoTome optical sectioning acquisition. There is one 2D image ("slice") for each axial depth; the slices form a stack representing the sample volume, as in Figure 1. Figure 7 shows the middle slices from four widefield image stacks from the brine shrimp sample; three stacks were acquired by using different excitation filters to shift the illumination wavelength, and the fourth stack contains composite images created by overlaying the images from the first three stacks.

Each excitation filter exposes different regions of the sample; the part that gets excited and consequently reflects light at a different wavelength. The images appear somewhat blurry; all the image restoration methods attempt to improve the clarity of these images by removing noise and adjusting out-of-focus light so more of it is in focus.

When the sample was acquired, care was taken to not introduce any errors into the output images. However, the range of depths acquired was too small, resulting in some light not being captured; this is clear from the XZ view (Figure 8a), as the light extends past the top and bottom of the view. This error had effects on the point spread function (Figure 6), and therefore, the deconvolutions.

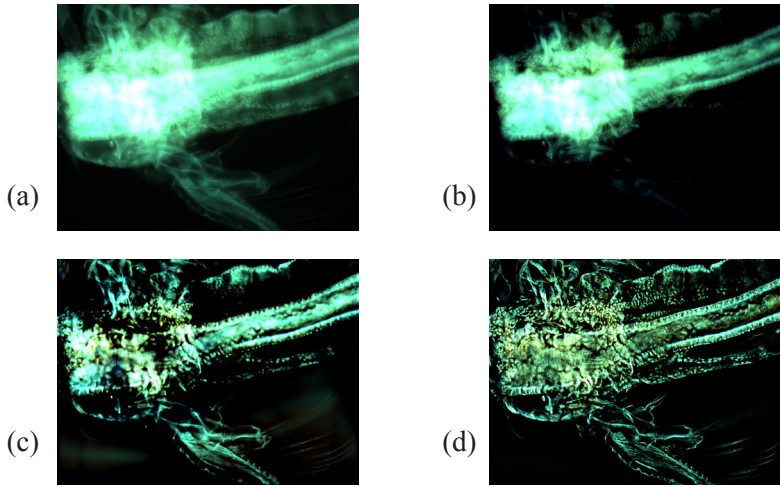


**Figure 8**.
XY views of the (a) raw widefield image, and restored images obtained using: (b) Nearest Neighbor, (c) Regularized Inverse Filter, and (d) CGML deconvolutions.

*Widefield Deconvolution*

Three deconvolution algorithms were applied to the raw widefield images. These are postprocessing methods that generate and attempt to remove the microscope's point spread function blurring effect from the acquired widefield data. Figure 8 and Figure 9, respectively, present the XY and XZ views from widefield and each algorithm for comparison. These images are composites of the three excitation filters used in the widefield acquisition.

Nearest Neighbor (Figure 8b) is the oldest and fastest 2D deconvolution algorithm provided in the ZEN software. It assumes that for each plane, the two immediate adjacent planes contribute the most information [3]. By removing convolved light from the nearest neighboring planes, an approximation of the plane of interest can be obtained. Only two 2D convolution operations need to be processed for each plane.

The Nearest Neighbor 2D deconvolution was performed using ZEN's default parameters. Compared to the widefield image (Figure 8a), there are less regions visible, but the regions that are visible appear mostly the same.

Regularized Inverse Filter (RIF, Figure 8c) is the next-fastest deconvolution algorithm in ZEN [16]. Unlike Nearest Neighbor, it performs a 3D deconvolution, and it attempts to mitigate the effects of noise on the

inverse image (the widefield output) by applying a denoising filter (regularization) before deconvolution.

The RIF deconvolution was performed using ZEN's default parameters, including the Zero Order regularization model and an automatically set strength. Comparing their orthogonal views of the XZ axis (Figure 9), the RIF deconvolution was able to restore more in-focus light than Nearest Neighbor.

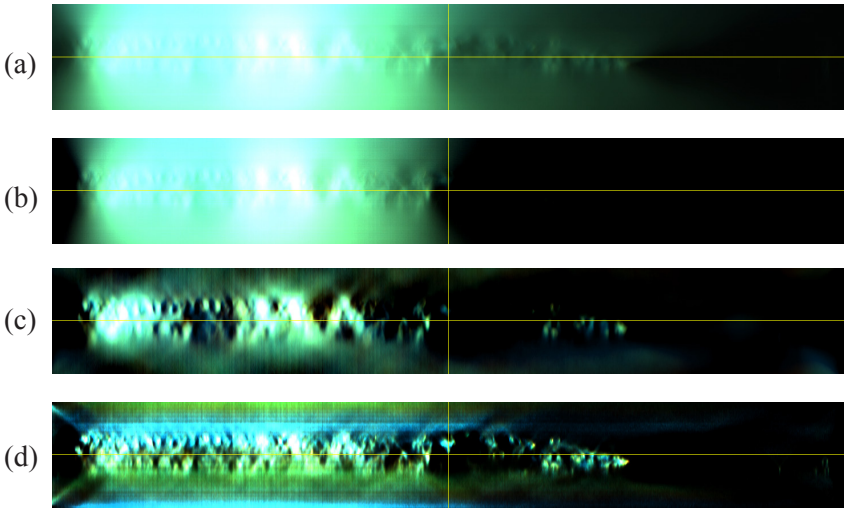


**Figure 9**.
XZ views of the (a) widefield image, and restored images obtained using: (b) Nearest Neighbor, (c) Regularized Inverse Filter, and (d) CGML deconvolutions.

The Conjugate Gradient Maximum Likelihood (CGML, Figure 8d) algorithm, unlike the others presented here, is an iterative method; the same steps are repeated multiple times until a satisfactory result is obtained based on a metric. In general, in each iteration, an estimate of the sampled object is convolved with the PSF and compared to the widefield image [5]. The percent error, the difference between the convolved estimate and widefield images, is used to generate a new estimation of the sample with reduced error. To aid in estimation, a non-negativity constraint is applied on the estimation, which means no pixel can have an intensity below zero, consistent with the fluorescence intensity in the sample.

This CGML deconvolution was performed with a maximum of 100 iterations per excitation filter, though only the result from the DAPI filter

data used that many. For the result from the Rhodamine data, 78 iterations were used, and for the EGFP result, 92. The algorithm is designed to stop when the percent error is satisfactory, or it cannot be decreased further. Comparing the images in Figure 8, it is clear that the CGML result (Figure 8d) contains the most detail.

The different results are also compared by their XZ views (Figure 9). These orthogonal images allow the depths (z-axis) of each image stack to be visualized. These XZ views are focused on Y = 520, which is the horizontal center of each XY view. X increases from left to right, and Z increases from top to bottom. The improvements to the XZ view mirror the improvements to each XY view. Nearest Neighbor (Figure 9b) restores some light but otherwise looks similar to widefield (Figure 9a). RIF (Figure 9c) improves upon Nearest Neighbor by removing much of the blur and returning light to the in-focus region. In CGML (Figure 9d), more in-focus light is visible, though artifacts can be seen in the out-of-focus regions (the top and bottom of the image).

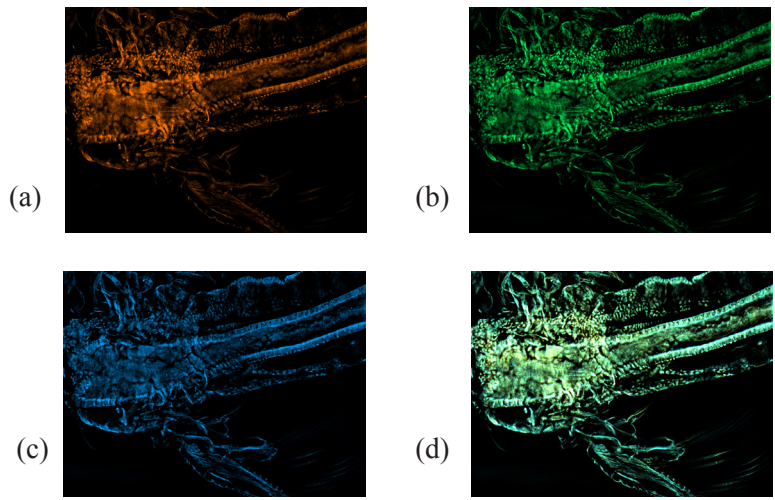


**Figure 10**.
XY view of the CGML deconvolution. (a) Rhodamine, (b) EGFP, (c) DAPI excitation filters, and (d) composite image of the three filters.

Figure 10 is a breakdown of the CGML image in Figure 8d, showing the result of each excitation filter alongside the composite image. The improvements observed in the composite image are present in each channel (compare to the widefield images in Figure 7).

*Structured Illumination Microscopy*

Structured illumination microscopy (SIM) datasets are reconstructions of an object captured using the optical sectioning capabilities of the ApoTome.2 add-on hardware. Optical sectioning is enabled by projecting a structured illumination (SI) pattern onto the captured images. The SI pattern modulates the illumination from the microscope's lamp so that the captured image will have light and dark sections corresponding to the structured light (Figure 3b); the light portions modulate (multiply) the in-focus information present in the slice [7]. By changing the lateral position (phase) of the pattern, the SI pattern multiples different portions of the image that are in focus.

In this study, the entire volume of the sample was imaged, and five phase images were captured for each slice. Each phase image contains a shifted version of the same sinusoidal grid pattern overlay. The different phase images are subtracted from each other, then the differences are squared and summed. Finally, the square root of the sum is taken, resulting in an image in which the grid pattern is removed along with the out-of-focus light, creating a new SIM-reconstructed image containing only the optically sectioned (in-focus) portions of each phase image [7].

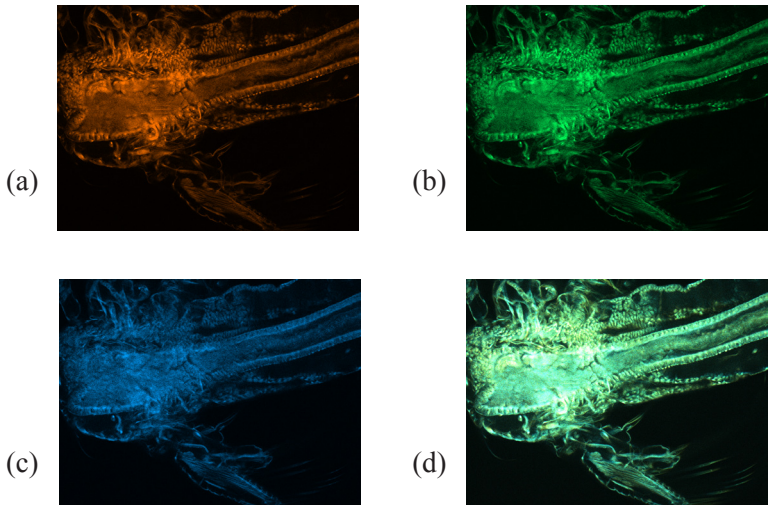


**Figure 11**.
XY views from the acquired and processed optically sectioned SIM image stack for: (a) Rhodamine, (b) EGFP, (c) DAPI excitation filters, and (d) composite image of the three filters.

ZEN's algorithm also applies corrections to prevent errors from the acquisition (unstable illumination, incorrect pattern positions, bleaching, etc.) from affecting the reconstruction as much as in deconvolution [17]. The effects of this computational approach of ApoTome SIM on the sample data can be seen in Figure 11.

Not only are the SIM images (Figure 11) less blurred than the widefield images (Figure 7), but they also display similar details as in the CGML images (Figure 10). The head (center left) of the sample and the whiskers (bottom middle) are much clearer in the SIM reconstruction than the widefield images, yet the result is still different from CGML due to the different processes involved. The next section contains more detailed analyses of the widefield, CGML, and SIM images.

*Qualitative Comparison*

Using the tools featured in Fiji [13], this study compares the widefield, CGML, and SIM images to determine each image restoration method's advantages and disadvantages. Figure 12 shows the XY views of the middle slice from each stack.

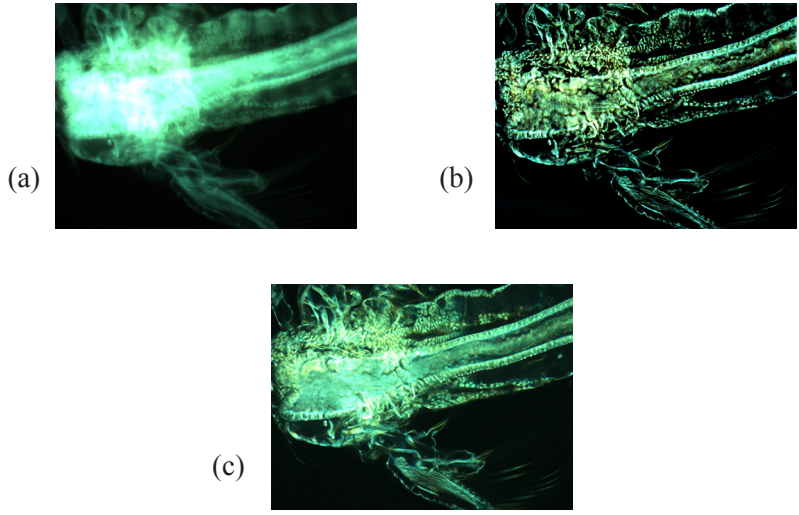


**Figure 12**.
XY views from the (a) widefield, (b) CGML, and (c) SIM image stacks (composite image of the three excitation filters).

Compared to the widefield slice, the CGML and SIM slices display the brine shrimp's structures in much greater detail. In particular, the head of the shrimp (left center) was completely blurred in the widefield slice; both restorations are sharper in that area. The CGML and SIM slices provided similar, yet slightly different views of the subject. CGML appears to contain more contrast in the structures, but without knowledge of the sample's true appearance, neither restoration can be objectively ruled as more accurate. Differences can also be seen in the XZ views, shown in Figure 13.

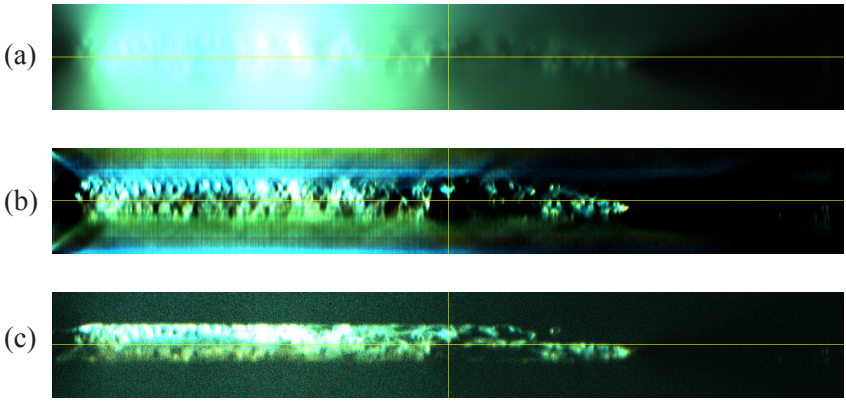


**Figure 13**.
XZ views from the (a) widefield, (b) CGML, and (c) SIM image stacks (composite image of the three excitation filters).

For each orthogonal view, in-focus light appears near the center of the sample (marked by the yellow horizontal line). In the widefield view, there is a lot of light above and below the in-focus region. In the CGML view, there is less blurring and more detail in the in-focus region, and the light in the out-of-focus region is also less blurred, though still present due to some artifacts. The SIM view appears to smooth out the in-focus region by having more light in the region but also lower contrast in the structures. The out-of-focus light is less prominent, with only some slight bleaching present. There is a progression in image quality from raw widefield to processed widefield, with SIM having a mixture of positive and negative differences.

*Quantitative Comparison*

Changes in pixel data within a certain region of the image can be visualized by intensity line plots, which plot a gray pixel value (of an arbitrary unit) against distance within the image of the sample. The lowest possible

intensity value (0) appears black, and the highest possible value appears white. Each image restoration method has a different result, so an intensity plot from the same region will look different for each case.

In this study, the intensity plots were created in Fiji [13]. A yellow line is drawn over the measured pixels, and the graph plots each pixel's intensity (referred to as "Gray Value" in Fiji) against the distance in microns from the left endpoint of the line. For easier viewing of intensities, images are presented in grayscale. Figure 14 shows an intensity plot from a widefield image.

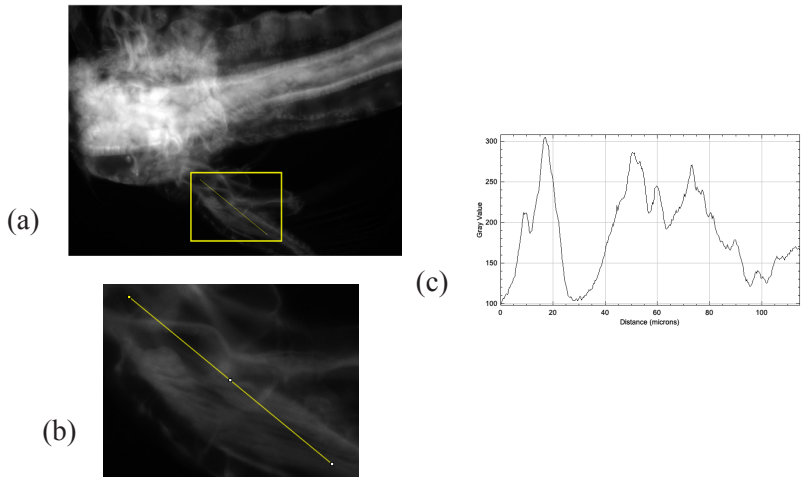


**Figure 14**.
(a) XY view from the widefield image stack (DAPI filter). (b) Crop from (a) shown by the yellow rectangle, focused on the 115 micron-long line overlay. (c) Intensity plot across the line overlay.

Figure 14c plots pixel intensity values against the distance of the line in Figure 14b. The widefield image uses 12 bits to store pixel data, so the maximum possible intensity value is $2^{12} - 1$, or 4,095. The pixels captured in this line overlay have values from 100 to 300. The plot contains smooth curves, which is expected due to the blurring effects of the PSF of the biological sample features. It appears that many of the sample's details have been lost, and out-of-focus information (blur) creates smooth curves. Figure 15 shows a different intensity plot from the same region of the result obtained after processing with the CGML deconvolution method.

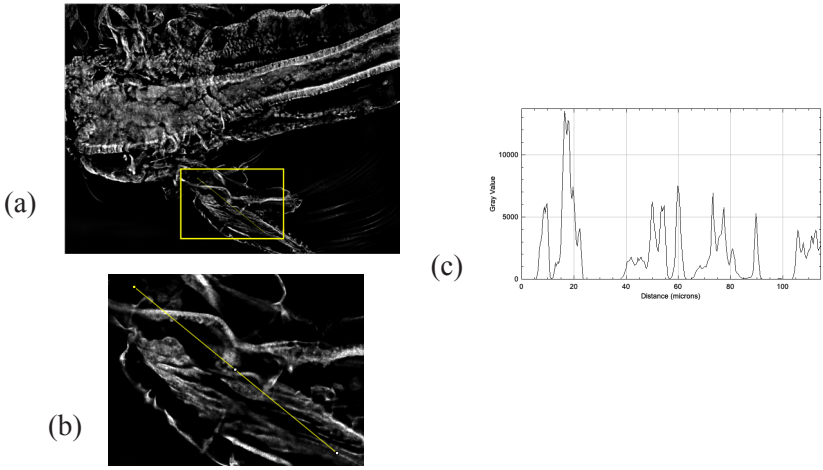


**Figure 15**.
(a) XY view from the CGML image stack (DAPI filter). (b) Crop of (a) shown by the yellow rectangle, focused on the 115 micron-long line overlay. (c) Intensity plot across the line overlay.

The results from the CGML deconvolution are 16-bit images, so the maximum intensity is $2^{16} - 1$, or 65,535. Much of the line selection shows an intensity of 0 (due to the algorithm's non-negativity constraint), but the peaks are better resolved (more peaks are visible, and they have defined maximums) and have values from roughly 5000 to 15000, which are higher compared to the widefield image. The deconvolution restores visual data (the relative brightness of each pixel). The peaks and curves are expected to be closer to the actual details in the sample, given the increased contrast and resolution in the image. Figure 16 shows a similar plot from the SIM image restoration.

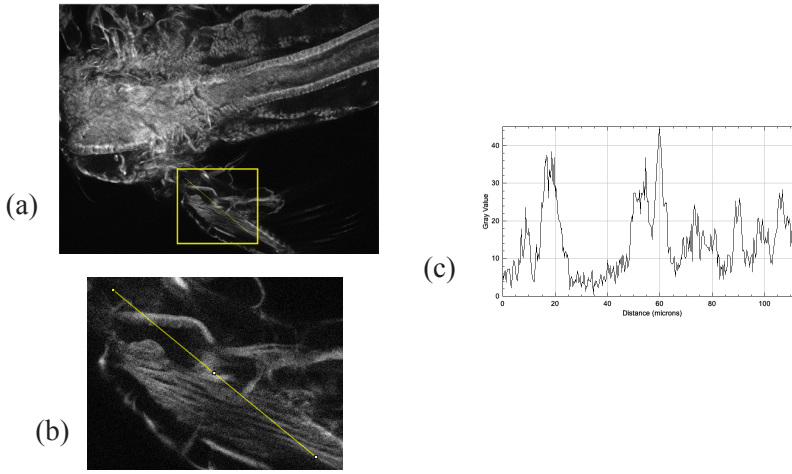


**Figure 16**.
(a) XY view from the SIM image stack (DAPI filter). (b) Crop of (a) shown by the yellow rectangle, focused on the 115 micron-long line overlay. (c) Intensity plot across the line overlay.

The SIM image, like the widefield image, is 12 bits, so the maximum intensity is 4,095, although the largest plotted intensity is much lower because SIM processing involves subtraction operations as part of the processing method [7]. As a result, the numerical data is lost, and the images appear more grainy or noisy than the CGML result. However, the pattern in this intensity plot is closer to the one in the CGML plot than the widefield plot, as the main peaks appear in the same locations. However, pixels that were zeroed out in CGML have values here, so more data is present in SIM, which could still be residual blur, as fewer peaks are identified. Additionally, there is more variation in the value of adjacent pixels, which better matches expectations when data is noisy. Although SIM and CGML XY images look similar, it appears that the CGML deconvolution provides an image with higher contrast, more resolution, and less noise than the SIM image.

## Discussion

Overall, both widefield deconvolution microscopy (through the CGML algorithm) and optically sectioned structured illumination microscopy (OS-SIM, powered by ApoTome.2) were effective methods to restore an image of a fluorescent biological sample. CGML and SIM had similar results when applied to the experimental widefield image, with CGML having the greater contrast. However, OS-SIM outperforms CGML in process-

ing time and ease of use. The ApoTome acquisition and the simpler SIM computations finished in minutes instead of the several hours necessary for the iterative computations of the CGML method, although both processes would have been faster with a dedicated graphics card. Since no point spread function is required, OS-SIM is simpler for a layperson to operate; by contrast, deconvolution has many more parameters to adjust. Also, SIM is a per-slice operation, so a selected number of slices can be optically sectioned and processed. Deconvolution requires a large z-axis to be effective, which is apparent by the artifacts in the reconstructions (Figure 9). However, deconvolution does not require any additional hardware, and many open-source software implementations are available, so it is a much less expensive alternative restoration method to ApoTome SIM for experienced researchers. Otherwise, some training is required.

## Conclusion

Three products from ZEISS Microscopy – the Axio Imager.Z1 microscope, the ApoTome.2 add-on hardware, and the ZEN imaging software – were used to acquire images from a fluorescent biological sample and perform several image restorations to make the images appear closer to the underlying object. No definitive conclusion could be made regarding the best restoration method since the true appearance of the sample is unknown; however, both SIM and CGML performed acceptably, and each could be used for different circumstances.

Most importantly, this study demonstrates two powerful techniques that have been developed over the last three decades to image 3D fluorescent samples and have been applied successfully to fields ranging from biology to health sciences. The two techniques appear in the literature for research studies that rely on close examination of fluorescent (naturally or otherwise) subjects, such as microorganisms or plant and animal cells. The brine shrimp sample here was used for training and demonstration purposes. The latest hardware and software are not necessary: the Axio Imager.Z1 and ApoTome.2 have been discontinued, and ZEN 3.8 is outdated, yet these tools worked here. Researchers that aim to use these products do not need to be experts in microscopy, either; however, they need to receive training and learn how deconvolution works. This study was performed by an undergraduate student who hopes to be able to use this knowledge to image samples for a collaborative biological study in the future.

## Acknowledgement

I, David Adaway, would like to thank the National Science Foundation (NSF) for funding my research as part of the VIP Program (NSF-IUSE award #2120819) as well as the Helen Hardin Honors College for providing a fellowship grant allowing me to work during the summer of 2024. I am grateful to Dr. Chrysanthe Preza for her supervision in conducting the work and writing this paper, and for the training she provided so that I can use her research facilities, where I conducted this study. I would like to thank Carl Zeiss Microscopy, Inc, for providing me with a demo dongle for ZEN so that I could conduct this experiment. I would also like to thank Mr. Lutz Schaefer of AIMC, Inc, and consultant for ZEISS Microscopy, who has authored several of the cited works ([2], [5], [10], [17]) and has provided accurate vectorial PSFs, which allowed me to obtain a high-quality CGML deconvolution result. His expertise and useful discussions were instrumental in completing this study successfully.

## References


[1] J. W. Lichtman and J.-A. Conchello, “Fluorescence microscopy,” *Nat. Methods*, vol. 2, no. 12, pp. 910–919, Dec. 2005, doi: 10.1038/nmeth817.

[2] W. Wallace, L. H. Schaefer, and J. R. Swedlow, “Digital Image Processing - Introduction to Deconvolution,” Olympus Life Science. Accessed: Jan. 04, 2025. [Online]. Available: https://www.olympus-lifescience.com/en/microscope-resource/primer/digitalimaging/deconv olution/deconintro/

[3] D. A. Agard, “Optical Sectioning Microscopy: Cellular Architecture in Three Dimensions,” *Annu. Rev. Biophys. Bioeng.*, vol. 13, no. 1, pp. 191–219, Jun. 1984, doi: 10.1146/annurev.bb.13.060184.001203.

[4] J.-B. Sibarita, “Deconvolution Microscopy,” in *Microscopy Techniques*, J. Rietdorf, Ed., Berlin, Heidelberg: Springer, 2005, pp. 201–243. doi: 10.1007/b102215.

[5] W. Wallace, L. H. Schaefer, and J. R. Swedlow, “A Workingperson’s Guide to Deconvolution in Light Microscopy,” *BioTechniques*, vol. 31, no. 5, pp. 1076–1097, Nov. 2001, doi: 10.2144/01315bi01.

[6] “Point Spread Function (PSF),” Scientific Volume Imaging. Accessed: Jan. 12, 2025. [Online]. Available: https://svi.nl/Point-Spread-Function-%28PSF%29

[7] M. A. A. Neil, R. Juškaitis, and T. Wilson, “Method of obtaining optical sectioning by using structured light in a conventional microscope,” *Opt. Lett.*, vol. 22, no. 24, p. 1905, Dec. 1997, doi: 10.1364/OL.22.001905.

[8] T. B. Gines and M. W. Davidson, “Structured Illumination: ZEISS ApoTome,” ZEISS Microscopy Online Campus. Accessed: Jan. 12, 2025. [Online]. Available: https://zeiss-campus.magnet.fsu.edu/tutorials/opticalsectioning/apotome/indexflash.html

[9] K. R. Castleman, *Digital image processing*. in Prentice-Hall signal processing series. Englewood Cliffs, N.J: Prentice-Hall, 1979.

[10] L. H. Schaefer, D. Schuster, and H. Herz, “Generalized approach for accelerated maximum likelihood based image restoration ap-

plied to three-dimensional fluorescence microscopy," *J. Microsc.*, vol. 204, no. 2, pp. 99–107, Nov. 2001, doi: 10.1046/j.1365-2818.2001.00949.x.

[11] S. F. Gibson and F. Lanni, "Experimental test of an analytical model of aberration in an oil-immersion objective lens used in three-dimensional light microscopy," *J. Opt. Soc. Am.A*, vol. 9, no. 1, p. 154, Jan. 1992, doi: 10.1364/JOSAA.9.000154.

[12] J. Kim, T. Li, Y. Wang, and X. Zhang, "Vectorial point spread function and optical transfer function in oblique plane imaging," *Opt. Express*, vol. 22, no. 9, pp. 11140–11151, May 2014, doi: 10.1364/OE.22.011140.

[13] J. Schindelin *et al.*, "Fiji: an open-source platform for biological-image analysis," *Nat. Methods*, vol. 9, no. 7, pp. 676–682, Jul. 2012, doi: 10.1038/nmeth.2019.

[14] C. A. Schneider, W. S. Rasband, and K. W. Eliceiri, "NIH Image to ImageJ: 25 years of image analysis," *Nat. Methods*, vol. 9, no. 7, pp. 671–675, Jul. 2012, doi: 10.1038/nmeth.2089.

[15] M. Linkert *et al*., "Metadata matters: access to image data in the real world," *J. Cell Biol.*, vol. 189, no. 5, pp. 777–782, May 2010, doi: 10.1083/jcb.201004104.

[16] W. Wang and M. K. Ng, "Convex regularized inverse filtering methods for blind image deconvolution," *Signal Image Video Process.*, vol. 10, no. 7, pp. 1353–1360, Oct. 2016, doi: 10.1007/s11760-016-0924-3.

[17] L. H. Schaefer, D. Schuster, and J. Schaffer, "Structured illumination microscopy: artefact analysis and reduction utilizing a parameter optimization approach," *J. Microsc.*, vol. 216, no. 2, pp. 165–174, Nov. 2004, doi: 10.1111/j.0022-2720.2004.01411.x.